Article

A Bulk Oxygen Vacancy Dominating WO_{3-x} Photocatalyst for Carbamazepine Degradation

Weiqing Guo [1], Qianhui Wei [1], Gangrong Li [1], Feng Wei [1,*] and Zhuofeng Hu [2,*]

1   GRINM (Guangdong) Institute for Advanced Materials and Technology, Foshan 528000, China; guoweiqing@grinm.com (W.G.); weiqianhui@grinm.com (Q.W.); ligangrong@grinm.com (G.L.)
2   Guangdong Provincial Key Laboratory of Environmental Pollution Control and Remediation Technology, School of Environmental Science and Engineering, Sun Yat-sen University, Guangzhou 510006, China
*   Correspondence: weifeng@grinm.com (F.W.); huzhf8@mail.sysu.edu.cn (Z.H.)

Abstract: Creating oxygen vacancy in tungsten trioxide (WO_3) has been considered as an effective strategy to improve the photocatalytic performance for degrading organic pollutants. In this study, oxygen vacancies were introduced into WO_3 by thermal treatment under Ar atmosphere and their proportion was changed by setting different treatment times. WO_{3-x} samples show better photoelectric properties and photocatalytic degradation performance for carbamazepine (CBZ) than an oxygen-vacancy-free sample, and WO_{3-x} with the optimal proportion of oxygen vacancies is obtained by thermal treatment for 3 h in 550 °C. Furthermore, it discovers that the surface oxygen vacancies on WO_{3-x} would be recovered when it is exposed to air, resulting in a bulk oxygen vacancy dominating WO_{3-x} (bulk-WO_{3-x}). The bulk-WO_{3-x} exhibited much higher degradation efficiency for CBZ than WO_{3-x} with both surface and bulk oxygen vacancies. The mechanism study shows bulk-WO_{3-x} mainly degrades the CBZ by producing OH radicals and superoxide radicals, while oxygen-vacancy-free sample mainly oxidizes the CBZ by the photoexcited hole, which requires the CBZ to be adsorbed on the surface for degradation. The radical generated by bulk-WO_{3-x} exhibits stronger oxidizing capacity by migrating to the solution for CBZ degradation. In summary, the influence of oxygen vacancy on photocatalytic degradation performance depends on both the proportion and location distribution and could lie in the optimization of the photodegradation mechanism. The results of this study could potentially broaden our understanding of the role of oxygen vacancies and provide optimal directions and methods for oxygen vacancy regulation for photocatalysts.

Keywords: tungsten trioxide; oxygen vacancy; photocatalytic degradation

1. Introduction

Along with industrialization and urbanization, organic pollutants have caused severe environmental problems and resulted in increasingly severe shortage of water resources [1]. Therefore, there is urgent demand for developing new techniques for resolving the problem of organic pollutants. In the past decades, research attention has been focused on developing and cost-effective photocatalytic technique as it is a green and efficient approach for degradation of organic pollutants [2–7]. In a photocatalytic degradation system, photocatalyst plays a vital role in the degradation efficiency of pollutants. Among all investigated photocatalysts, tungsten trioxide (WO_3) exhibits a competitive advantage for the degradation of organic pollutants. Owing to its relatively narrow band gap (2.4–2.8 eV) and positive valence band (VB), WO_3 can utilize visible light energy and have stronger oxidation ability [8,9]. They are both beneficial to oxidize organic pollutants. However, WO_3, as a photocatalyst, also has the shortcomings of low photogenerated carries density, poor charge transfer efficiency and electron–hole separation [9].

Previous studies have suggested that introducing defect structure into WO_3 could be an effective way to overcome the above shortcomings, and oxygen vacancy is a simple

but effective defect structure for improving the photocatalytic performance of WO_3 [10]. According to the previous literature, the promotion from oxygen vacancy can be reflected in several aspects. Some research demonstrates that oxygen vacancy improves the utilization of light energy due to extending light absorption of WO_3 in the visible regions [11]. Some studies demonstrated that oxygen vacancy can effectively promote the separation of photogenerated electron–hole so that it can maximize the utilization rate of photogenerated carriers [12]. Other reports verify that the existence of oxygen vacancy can increase the charge transfer efficiency [13]. However, some reports showed that oxygen vacancies could cause negative influence on the photocatalytic performance because they may act as traps for photogenerated charge carriers [14], become recombination centers of electron and hole and weaken the crystal structure [15].

Oxygen vacancies can be introduced to WO_3 by thermal treatment in inert or reducing atmosphere [16–19]. It is investigated whether thermal treatment with different atmospheres, temperatures or durations can result in different impacts on the distribution of oxygen vacancies and, thereby, the photocatalytic performance. When the thermal treatment temperature rises from 350 °C to 550 °C, the formation rate of surface oxygen vacancies is fast at lower temperatures, but it would slow down at higher temperatures because of the migration of oxygen atoms from bulk phase to surface [20]. Higher temperatures may be more conducive to the formation of bulk oxygen vacancies. It is considered that surface and bulk oxygen vacancies generated by thermal treatment play different roles on photocatalytic performance of samples [9]. Bulk oxygen vacancies could format intermediate electronic bands [21,22], which can inhibit the recombination of photogenerated electron–hole pairs [23,24]. Meanwhile, surface oxygen vacancies could result in a decrease in VB due to the local band caused by surface defect [25,26]. In addition, wet chemical reduction, including sol-gel method [27] and solvothermal method [28], and electrochemical reduction [29] are also investigated to construct oxygen vacancies in WO_3.

This study aims to investigate the influence of oxygen vacancies on the photocatalytic degradation performance of WO_3. Here, carbamazepine (CBZ) will be used as a representative pollutant for studying their photocatalytic degradation performance. The proportion of introduced oxygen vacancies into WO_3 are changed by setting different thermal treatment times under Ar atmosphere and optimized by analyzing their structures and morphology properties, photoelectrochemistry properties and photocatalytic degradation performance for CBZ. Furthermore, the influence of oxygen vacancy location is also considered by comparing the WO_{3-x} samples with different distributions of surface and bulk oxygen vacancy. Finally, the CBZ degradation mechanism by WO_3 and optimized WO_{3-x} are investigated.

2. Materials and Methods

2.1. Preparation of Pristine WO_3 and WO_3 with Oxygen Vacancies

A pristine WO_3 sample was prepared by a hydrothermal method, referring to reported reference [30]. First, 210 mg of sodium tungsten (Na_2WO_4, Sigma-Aldrich, Burlington, MA, USA) was dissolved in 30 mL of deionized (DI) water. Then, 10 M hydrochloric acid (HCl, Fischer Scientific, Waltham, MA, USA) was added dropwise into the solution until it became turbid, followed by the addition of 210 mg of ammonium oxalate (($NH_4)_2C_2O_4$, Sigma-Aldrich, Burlington, MA, USA) into the mixture. After 10 min of stirring, the turbid solution became clear and was then transferred into a Teflon-lined stainless-steel autoclave, which was sealed and heated at 120 °C for 12 h. After that, the resulting yellow powder was filtered and washed with ethanol and water. The yellow powder was $WO_3 \cdot H_2O$ and transformed into WO_3 after being calcinated at 550 °C for 3 h.

WO_{3-x} samples: the pristine WO_3 nanoparticles were thermally treated in pure Ar flow at 550 °C for 0.5 h, 3 h, 6 h or 10 h to prepare four WO_{3-x} samples, which were denoted as WO_{3-x}-0.5 h, WO_{3-x}-3 h, WO_{3-x}-6 h or WO_{3-x}-10 h samples, respectively.

2.2. Preparation of Pristine WO$_3$ and WO$_3$ with Oxygen Vacancies

Scanning electron microscopy (SEM) images were taken on a Quanta 400 Thermal FE environmental scanning electron microscope (FEI, Eindhoven, The Netherlands). The diffuse reflectance absorption spectra of the samples were obtained by a UV-visible spectrophotometer equipped with an integrated sphere attachment (UV-3600, SHIMADZU, Kyoto, Japan). The X-ray diffraction (XRD) data were recorded on a Rigaku diffraction instrument using a Cu Kαradiation source with λ = 0.15418 nm (SmartLab, Rigaku, Tokyo, Japan). Photoelectrochemistry (PEC) measurements were performed on an electrochemical workstation (CHI760E, Chenhua, Shanghai, China) equipped with a three-electrode cell. The working electrode was made as follows: 2 mg of samples was fixed on FTO conducting glass mixed with 0.05 mL 0.05 wt% Nafion (Sigma-Aldrich, Gillingham, Dorset, UK), using graphite rod as counter electrodes and Ag/AgCl as the reference electrodes, and 0.1 M Na$_2$SO$_4$ was used as the electrolyte. The EPR spectra were detected by a CW/Pulse EPR system (A300, Bruker Co., Bremen, Germany) with a microwave frequency of 9.64 GHz, a microwave power of 0.94 mW, a modulation frequency of 100 kHz and a modulation amplitude of 2.0 G. X-Ray photoelectron spectroscopy (XPS) was performed using a Thermo Fisher Scientific K-Alpha (Thermo Scientific, Waltham, MA, USA) equipped with a VG CLAM 4 MCD electron energy analyzer (Thermo Scientific, Waltham, MA, USA) and twin-anode Mg Kα radiation (1253.6 eV) or Al Kα radiation (1496.3 eV) X-ray sources.

2.3. Photocatalytic Performance Experiments

All photocatalytic degradation experiments were carried out in a quartz tube, with 0.25 g/L photocatalyst and 5 ppm carbamazepine (CBZ, Macklin, Shanghai, China) under ultraviolet-visible irradiation from a 35 W xenon lamp. The control measurement of CBZ under illumination was tested as the blank sample. At an interval of 20 min, 0.5 mL of the solution was extracted. The residual concentrations of CBZ in reaction solution were detected every 20 min by HPLC (Shimadzu LC-20AD, Shimadzu Corporation, Kyoto, Japan) equipped with a Poroshell 120 EC-C18 column (4.6 mm × 100 mm, 2.7 μm, Agilent Technology, Santa Clara, CA, USA). The mobile phase for HPLC detection was a mixture of methanol and water with a ratio of 6:4 and at a 0.6 mL/min flow. The photocatalytic activity was evaluated using a time profile of C$_t$/C$_0$, where C$_t$ is the concentration of the pollutants at the irradiation time t and C$_0$ is the concentration at the equilibrium before irradiation, respectively.

2.4. Detection and Measurements of Photogenerated Radicals

The formed active oxygen radicals, including ·OH, ·O^{2-} and ^{1}O$_2$, in photocatalytic degradation systems were all identified by a Bruker A300 electron paramagnetic resonance (EPR) spectrometer (Billerica, MA, USA) using 5,5-dimethyl-1-pyrroline-N-oxide (DMPO), DMPO with methanol and TEMP as the trapping agent. Typically, 100 mM of DMPO was mixed with 20 mL solution (including 0.25 g·L^{-1} catalyst, 5 ppm CBZ). All samples had been illuminated for 5 min before ERP measurements.

3. Results and Discussion

3.1. Structures and Morphologies Properties

The SEM images show that the WO$_3$ powder particle is a cluster of two-dimensional nanosheets with the size of ca. 1 μm (Figure 1a,b). After being thermally treated for 0.5 h to 10 h, there is no remarkable visual change in particle surface morphology and size of the samples (Figure 1c–f), suggesting the morphology of WO$_3$ is stable.

Figure 2 shows the optical properties of all samples. As compared with untreated WO$_3$, the color of thermally treated WO$_3$ samples changed from yellow to olive-green (0.5 h and 3 h) and then to indigo after 6 h and 10 h thermal treatment (Figure 2a). According to the literature, the change in color could be attributed due to the formation of bulk oxygen vacancies [9]. Correspondingly, their light absorption in the visible regions is extended

with the increase in oxygen vacancy (Figure 2b). It can be found that more light can be absorbed when the WO_3 samples are thermally treated for a longer time. Figure 2c shows the band gap of the samples calculated by the linear approximation of $(\alpha h\nu)$ 2 vs. photo energy [31]. Visibly, all WO_{3-x} samples possess a narrower band gap than pristine WO_3 due to oxygen vacancy [9,22,32]. The calculated value of pristine WO_3 is around 2.77 eV, whereas the optical absorption of the WO_{3-x} samples gradually shifts to the longer wavelengths with the band gap value (*Eg*) ranging from 2.53 to 2.71 eV. Among all WO_{3-x} samples, WO_{3-x}-10 h shows the most intense light absorption and the narrowest band gap.
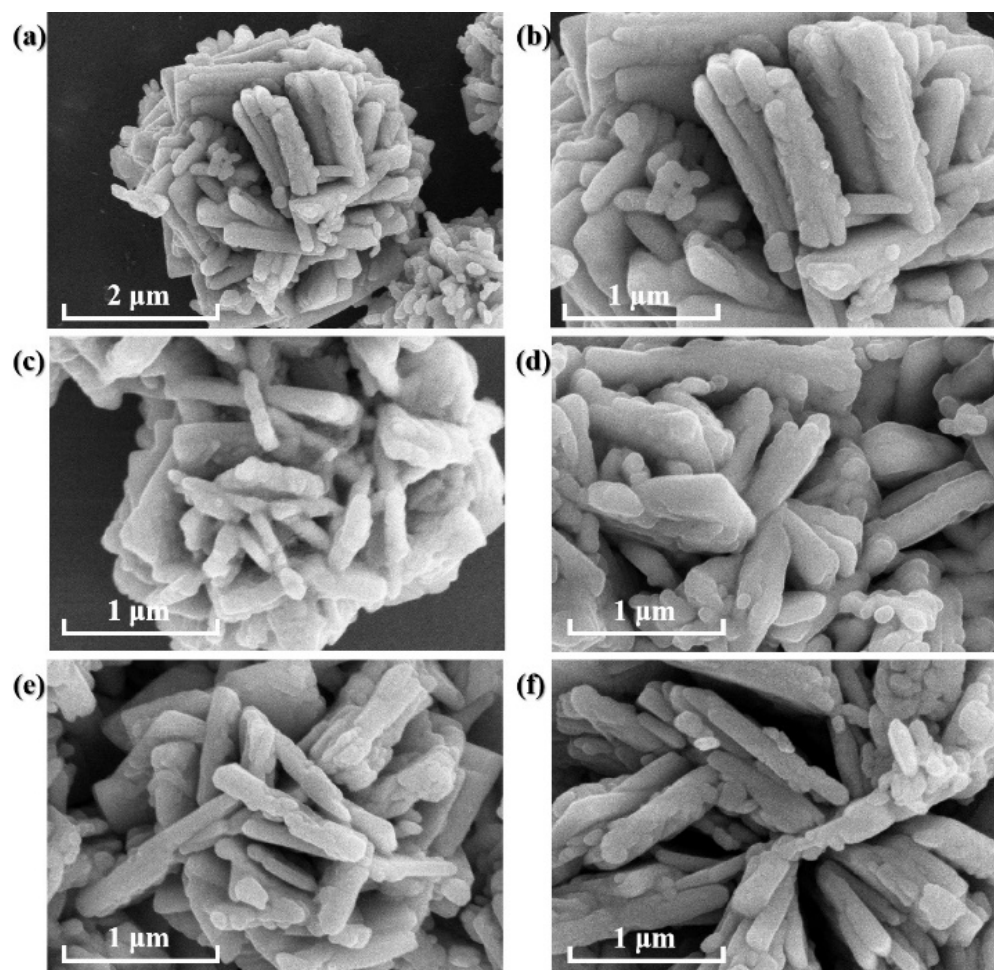
Figure 1. SEM images of (**a**,**b**) WO_3; and WO_{3-x} samples: (**c**) WO_{3-x}-0.5 h; (**d**) WO_{3-x}-3 h; (**e**) WO_{3-x}-6 h; (**f**) WO_{3-x}-10 h.

The XRD pattern (Figure 3a) of all samples could be indexed to the monoclinic phase of WO_3 (JCPDF20-1324). There is no observable shift for all characteristic diffraction peaks of WO_3 after thermal treatment. It suggests that the main crystal structure is preserved even though oxygen vacancy is increased [33]. Nevertheless, the intensity of the diffraction peaks slightly weakens with the increase in their thermal-treated time, indicating the degradation of the WO_3 crystallinity [34]. Crystalline degradation was mainly reflected in the orientations on (020), (022) and (202) planes (Figure 3b,c).

Based on the results of SEM, UV-vis diffuse reflectance spectra and XRD, it can be concluded that the introduction of oxygen vacancy has little influence on the surface morphology and size of WO_3, except narrowing its band gap and weakening its crystal structures.
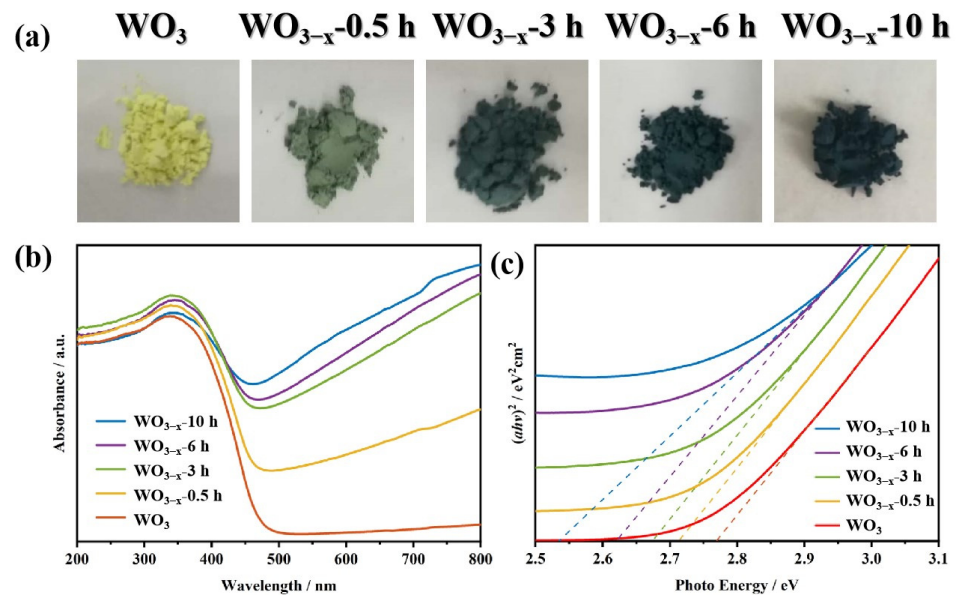
Figure 2. (**a**) The photographs; (**b**) UV-vis diffuse reflectance spectra; (**c**) band gaps calculated from Kubellka–Munk plots of the samples.
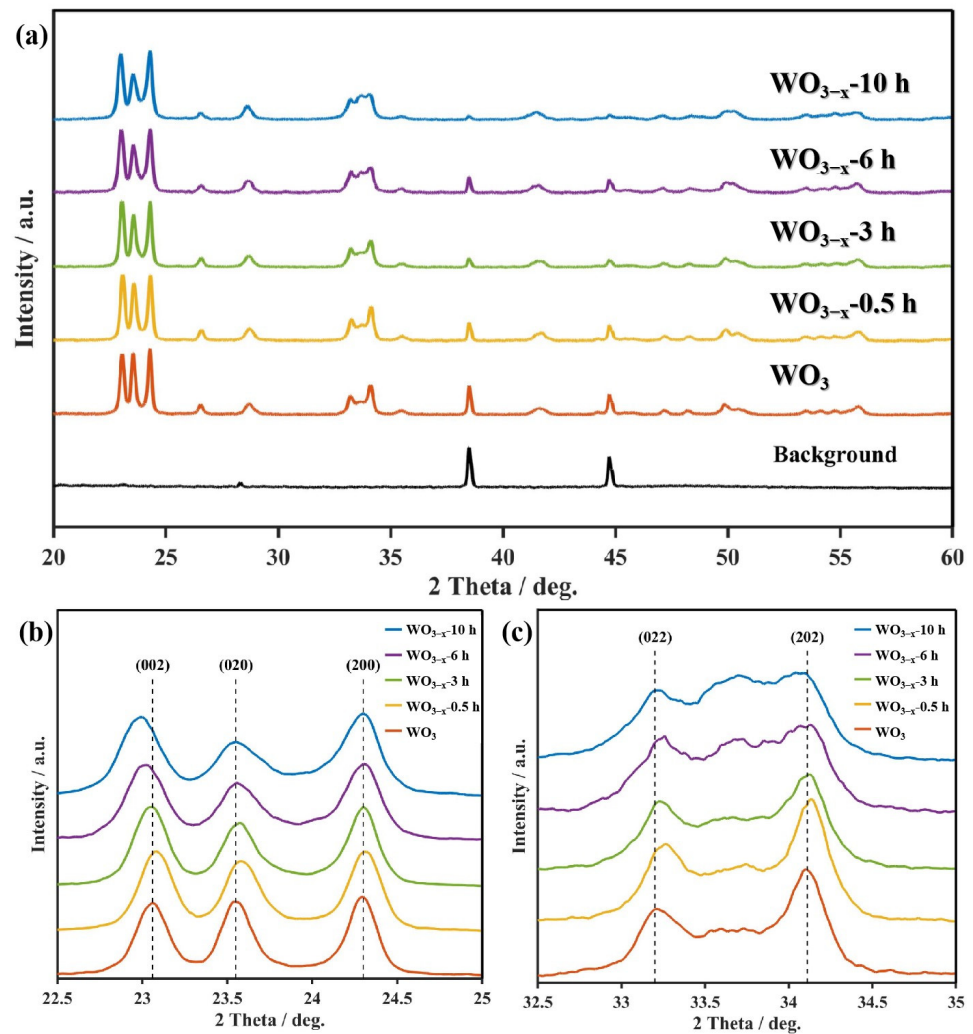
Figure 3. (**a**) XRD patterns of WO_3, WO_{3-x}-0.5 h, WO_{3-x}-3 h, WO_{3-x}-6 h and WO_{3-x}-10 h; (**b**) their XRD patterns on (002), (020) and (200) planes and (**c**) on (020) and (200) planes.

3.2. Photoelectrochemistry (PEC) Properties

PEC measurements were conducted in a three-electrode electrochemical cell in 0.1 M Na_2SO_4 solution (pH: ca. 7.0). The photocurrent density is measured at 0.6 V and the result is shown in Figure 4a. It illustrates that WO_{3-x} samples can produce higher photocurrent density than pristine WO_3, as reflected in the i-t patterns with on–off recycles of intermittent irradiation. This suggests that the introduction of oxygen vacancy, to some extent, can improve the photo-irradiated charge transfer efficiency of WO_3. The improvement is considered to come from WO_3/WO_{3-x} heterojunction formed by the energy difference between WO_3 and the oxygen-vacancy-rich layer [35]. Among all WO_{3-x} samples, WO_{3-x}-3 h exhibits the highest photocurrent density, which is about triple that of pristine WO_3 at 0.6 V vs. RHE. Nevertheless, the photocurrent density of WO_{3-x} samples decreases when the oxygen vacancies exceed the optimal proportion, indicating that the further increase in oxygen vacancies in WO_{3-x} is not necessary.
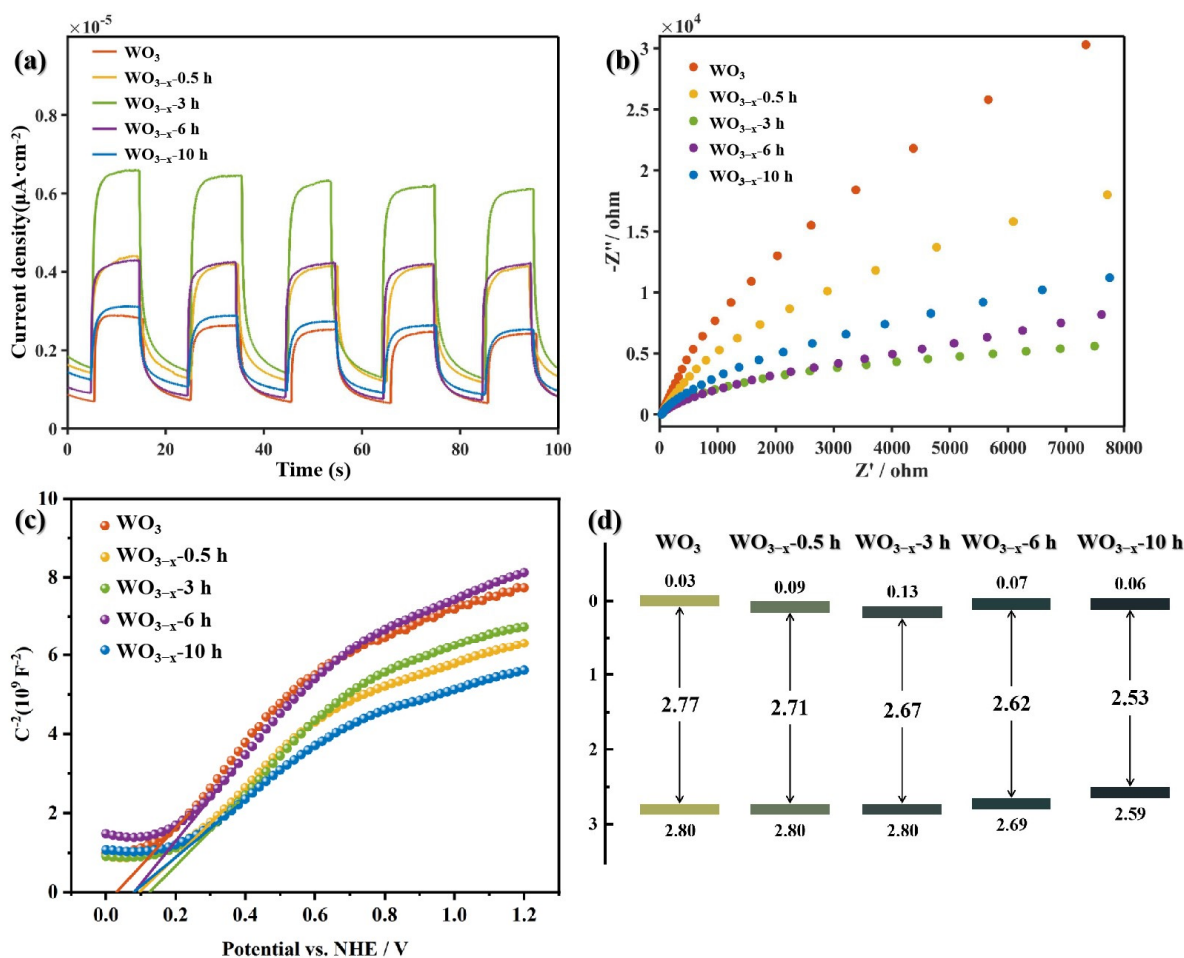
Figure 4. (**a**) Transient photocurrent responses; (**b**) EIS spectra; (**c**) Mott–Schottky plots; and (**d**) band structure diagram of as-prepared samples.

A similar trend has been observed in EIS, which is the common analytical tool to estimate charge separation and migration. As displayed in Figure 4b, four WO_{3-x} samples exhibit a smaller arc radius than pristine WO_3, verifying that the existence of oxygen vacancy can reduce interfacial charge transport resistance, thus leading to more effective charge separation. The charge transport resistance reached the minimum value when WO_3 had been thermally treated for 3 h. A trend from rising then declining generally means the charge transfer efficiency of WO_{3-x} samples suffers from two opposite (positive and negative) influence factors. Based upon the result of XRD (Figure 3), the negative influence may arise from the crystalline destruction when the samples have excessive oxygen vacancies.

As a result, the optimal proportion of oxygen vacancies appeared when WO_3 was thermal treated for 3 h and, thus, WO_{3-x}-3 h presents the best electrical performance.

The Mott–Schottky plots (Figure 4c) of pristine and WO_{3-x} samples are plotted according to ref [30,36,37]. The flat-band potentials are calculated to be 0.03, 0.09, 0.13, 0.07 and 0.06 V vs. NHE for WO_3, WO_{3-x}-0.5 h, WO_{3-x}-3 h, WO_{3-x}-6 h and WO_{3-x}-10 h, respectively. As their Eg were 2.77, 2.71, 2.67, 2.62 and 2.53 eV, their VB can be calculated according to the equation of $E_g = E_{VB} - E_{CB}$. The detail of band structures is illustrated in Figure 4d.

3.3. Photocatalytic Degradation of CBZ

The photocatalytic degradation of 5 ppm CBZ by as-prepared samples is investigated, and results are shown in Figures 5 and 6 and photocatalytic degradation efficiency (%) can be calculated by Equation (1) [38]. Here, C_t is the concentration of the pollutants at the irradiation time t and C_0 is the concentration at the equilibrium before irradiation, respectively.

$$\text{Degradation efficiency (\%)} = (1 - C_t/C_0) \times 100\% \quad (1)$$
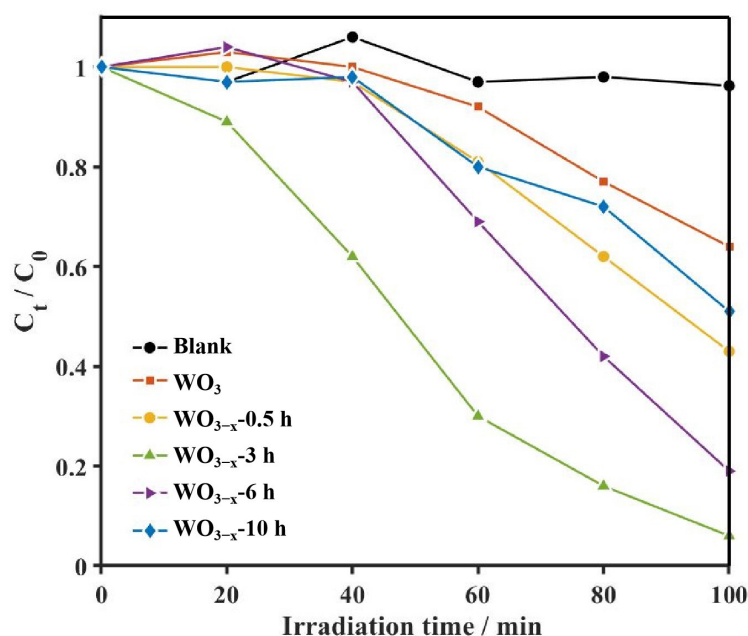
Figure 5. Photocatalytic degradation curve of as-prepared samples for CBZ under UV-vis.

As showed in Figure 5, only 36% CBZ has been removed by pristine WO_3 after 100 min, while those of the WO_{3-x} samples ranged from 49% to 94%. Obviously, the degradation efficiencies on WO_{3-x} samples are remarkably higher than that of pristine WO_3. Here, the kinetic constant (k) for CBZ is further estimated by the following equation [38]:

$$k = -\ln(C_t/C_0)/t \quad (2)$$

The plots of $-\ln(C_t/C_0)$ vs. t are found to be a linear relationship, clarifying that the photocatalytic degradation reaction of CBZ can be described by using a pseudo-first-order model (Figure S1). From the kinetic curves, the kinetic constant k values on WO_3 are calculated to 0.0060 min^{-1}, while those of WO_{3-x}-0.5 h, WO_{3-x}-3 h, WO_{3-x}-6 h and WO_{3-x}-10 h are increased to 0.0106, 0.0340, 0.0212 and 0.0081 min^{-1}, respectively (Figure 6a). Hence, the k value on WO_{3-x}-3 h was the largest and 5.67 times that of on WO_3, suggesting that the introduction of oxygen vacancy can significantly improve the photocatalytic degradation performance of WO_3. However, the photocatalytic performance of WO_{3-x} samples decreased when the oxygen vacancies exceeded the optimal proportion (WO_{3-x}-3 h). The

improved photocatalytic performance is considered to originate from the promotion of the dissociation of excitons and accelerates the transfer of charges.
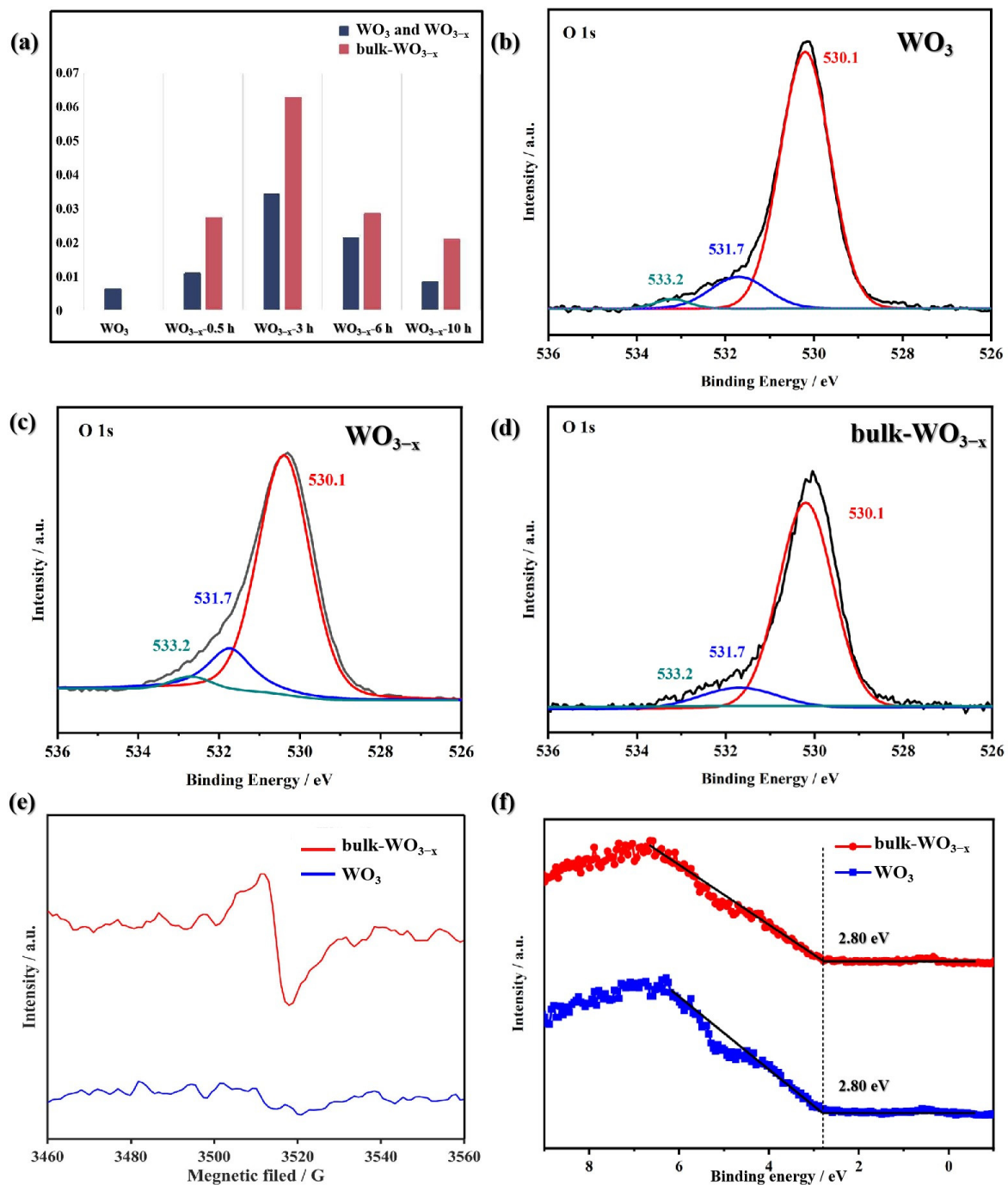
Figure 6. (**a**) Kinetic constant (k) of as-prepared samples for CBZ under UV-vis; O 1s XPS spectra of (**b**) WO_3, (**c**) WO_{3-x} and (**d**) bulk-WO_{3-x}; (**e**) EPR spectra and (**f**) VB XPS spectra of WO_3 and bulk-WO_{3-x}.

3.4. Optimization of Oxygen Vacancy

The activity of WO_{3-x} can also be enhanced by optimizing the oxygen vacancy location distribution. As mentioned above, the thermal treatment causes oxygen vacancies both in bulk and on surface and leads to higher activity. Interestingly, it was found that the sample would exhibit even higher activity when it was placed in the air for a period of time. This interesting phenomenon can presumably be attributed to the recovery of the surface

oxygen vacancies. It may produce bulk oxygen vacancy dominating WO_{3-x} samples, along with a decrease in surface oxygen vacancies, and, hence, these were named as bulk-WO_{3-x}. The degradation efficiency of bulk-WO_{3-x} is higher and their kinetic constant increases to 0.0271, 0.0628, 0.0284 and 0.0208 min^{-1}. They are 1.34~2.57 times that of WO_{3-x} just after thermal treatment. This indicates oxygen exposure of the thermally treated sample will exhibit higher activity as compared.

The surface oxygen vacancies can be investigated by XPS. Figure 6b–d show the O 1s XPS spectra of WO_3, WO_{3-x} (represented by WO_{3-x}-3 h) and bulk-WO_{3-x} (represented by bulk-WO_{3-x}-3 h) samples, which were deconvoluted in three peaks. The peaks at about 530.2, 531.7 and 533.2 eV correspond to surface lattice oxygen species (O_L), hydroxyl species (O_{OH}) and adsorbed water species (O_{H2O}), respectively. It is considered that the percentage of O_{OH} signal links to the quantity of surface oxygen vacancies [9,24,39]. The percentages of the three oxygen species of WO_3, WO_{3-x} and bulk-WO_{3-x} samples are listed in Table 1. Their percentage of O_{OH} increases obviously from 11.8% for WO_3 to 15.3% for bulk-WO_{3-x}, suggesting the thermal treatment causes surface oxygen vacancies.

Table 1. Detailed results of O 1s XPS spectra of pristine WO_3, OV-WO_3-3 h and bulk-OV-WO_3.

		Total	O_L	O_{OH}	O_{H2O}
	WO_3	84,376.662	72,615.110	10,022.600	1738.952
Area	WO_{3-x}	174,771.533	142,919.300	26,817.080	5035.153
	bulk-WO_{3-x}	78,938.520	64,014.520	8907.012	6016.988
	WO_3	100%	86.1%	11.8%	2.1%
Percentage	WO_{3-x}	100%	81.8%	15.3%	2.9%
	bulk-WO_{3-x}	100%	81.1%	11.3%	7.6%

Moreover, when the WO_{3-x} sample was placed in the air for a period of time, the density of surface oxygen vacancies decreases apparently. As shown in Table 1, the percentage of O_{OH} decreases from 15.3% to 11.3%. This demonstrates that many surface oxygen vacancies are recovered. It is reported that the surface oxygen vacancies will cause a shift of VB position [9,25,26]. However, the VB positions of WO_3 and bulk-WO_{3-x} samples are both 2.80 eV (Figure 6f), without any shift in VB positions between the two samples. It demonstrates that much of the surface oxygen vacancies are recovered and the density of surface oxygen vacancies in bulk-WO_{3-x} sample has become similar to that of pristine WO_3. Meanwhile, EPR spectra indicate the formation of bulk oxygen vacancies (Figure 6e). The EPR signal can still be observed on bulk-WO_{3-x} sample but there is no signal in the pristine WO_3 sample. It indicates the existence of bulk oxygen vacancy in the bulk-WO_{3-x} sample.

Therefore, it can be concluded that the activity of samples increases when both bulk and surface oxygen vacancies are presented, while the activity is further increased when the surface oxygen vacancies are recovered. The procedures of preparation from pristine WO3 to WO_{3-x} and bulk-WO_{3-x}. are exhibited as Figure 7.
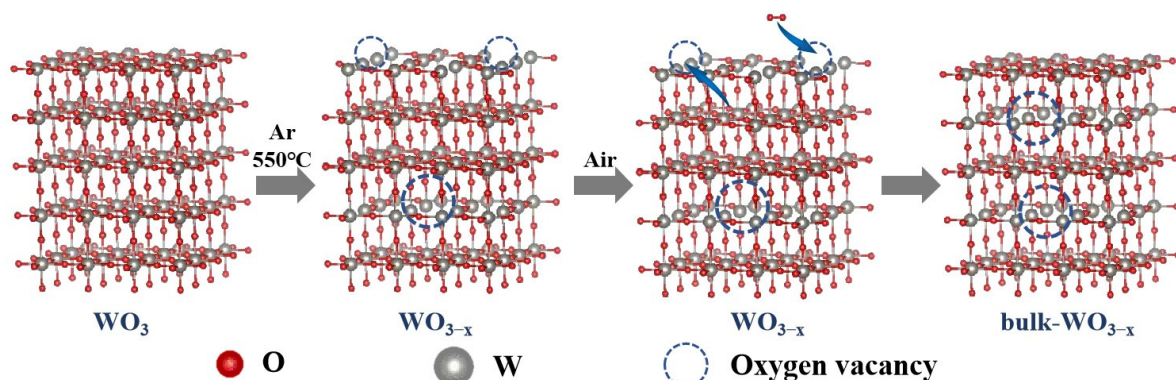
Figure 7. The schema of preparation from pristine WO_3 to WO_{3-x} and bulk-WO_{3-x}.

3.5. Mechanism of Photocatalytic Degradation

Inspired by this interesting phenomenon, the bulk oxygen vacancy dominating samples is considered as the optimal one for photocatalytic degradation. Subsequently, the mechanism for the degradation is studied.

To investigate the contribution of the various oxidative species generated in the photocatalytic system of WO_3 and bulk-WO_{3-x} samples for the degradation of CBZ, active species are tested by EPR. The generation of reactive oxygen species in the system are monitored though EPR technique after adding DMPO or TEMP as the trapping agent under UV-vis radiation. As shown in Figure 8a, a four-line EPR signal of DMPO-·OH adduct with an intensity ratio of 1:2:2:1 is also detected in both of WO_3 and bulk-WO_{3-x} systems, and the intensity of DMPO-·OH adduct signal in the system with WO_{3-x} is much stronger than that of WO_3. It indicates oxygen vacancy is significantly conducive to the generation of ·OH. As the VB of WO_3 and WO_{3-x} are both 2.80 eV, more positive than the standard redox potential of H_2O/·OH (2.37 V) [40], both samples can oxidize H_2O to ·OH under UV-vis thermodynamically. Therefore, ·OH can be generated from the oxidation of H_2O directly ($h^+ + H_2O \rightarrow$ ·OH + H^+). Then, methanol is added during the EPR measurement to catch ·OH and four very weak peaks with an intensity ratio of 1:1:1:1 are detected in bulk-WO_{3-x} with oxygen vacancies (Figure 8b). It suggests that ·O^{2-} is generated in bulk-WO_{3-x} systems, as they are the characteristic quartet signal of DMPO-·O^{2-} adduct. Here, ·O^{2-} may be generated by the reduction of O_2 ($e^- + O_2 \rightarrow$ ·O^{2-}). However, these characteristic signals cannot be observed in WO_3 systems without oxygen vacancies. Therefore, this strongly indicates that the introduction of oxygen vacancies is favorable for the formation of ·O^{2-}, which is beneficial to the degradation efficiency. In addition, there is no signal of TEMP-$^1O_2$ adduct detected in WO_3 nor bulk-WO_{3-x} systems (Figure 8c).
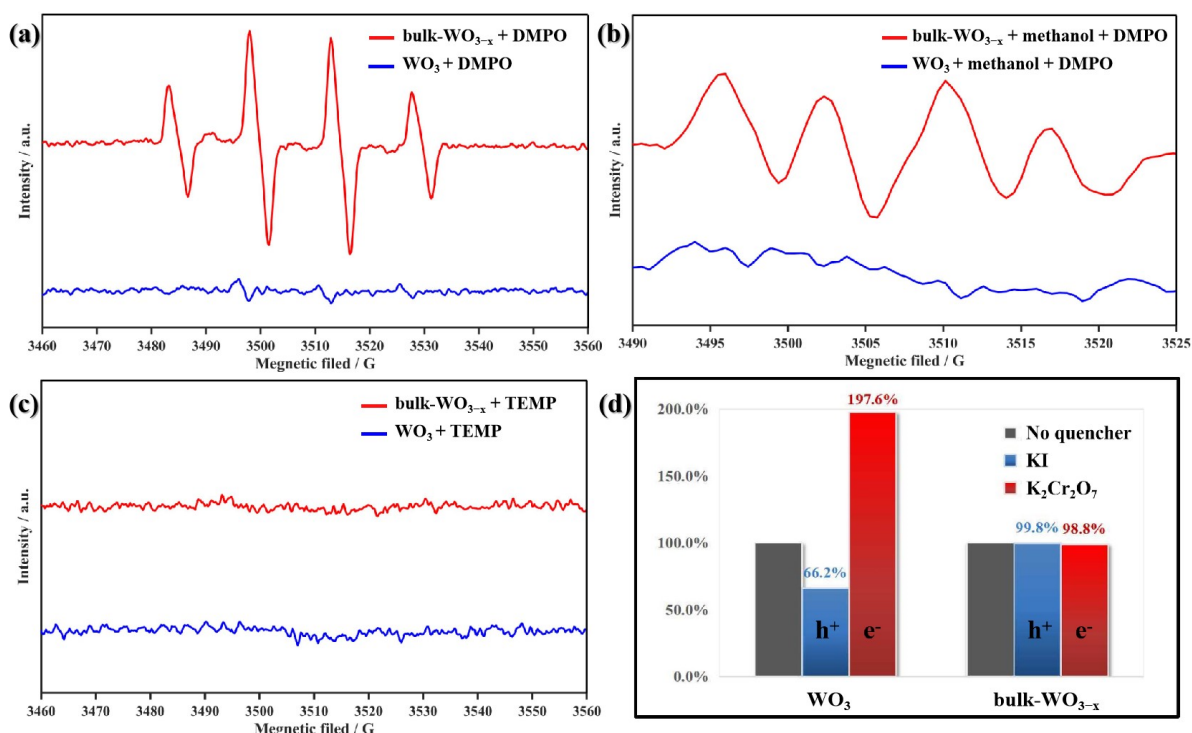
Figure 8. EPR spectra of (**a**) DMPO-·OH adduct; (**b**) DMPO-·O^{2-} adduct and (**c**) TEMP-$^1O_2$ for WO_3 and bulk-WO_{3-x} under UV-vis irradiation; (**d**) the changes in degradation efficiencies of CBZ in WO_3 and bulk-WO_{3-x} photocatalytic systems with KI or $K_2Cr_2O_7$ as quenchers.

In addition, active species trapping tests are also executed by adding KI and $K_2Cr_2O_7$ as the quenchers of photoexcited hole (h^+) and e^-, respectively. When 10 mM KI is added into the WO_3 system, the degradation efficiency of CBZ remarkably decreases to 66.2%

of pristine value (Figure 8d). It suggests that photoexcited hole (h^+) is one of the major reactive species contributing to the catalytic degradation of CBZ by WO_3. However, the addition of KI in the bulk-WO_{3-x} does not influence the degradation efficiency. This means that the hole does not directly cause the degradation of CBZ; instead, the hole mainly oxidized water into OH radicals for the degradation.

Meanwhile, the degradation efficiency of CBZ remarkably increase to 197.6% as compared with pristine value when 10 mM $K_2Cr_2O_7$ is added. The increase may originate from the promotion of charge separation due to quenching of e^-. In comparison, the degradation efficiency of CBZ in the bulk-WO_{3-x} photocatalytic system has little change by adding 10 mM $K_2Cr_2O_7$. This should be due to the high charge transfer efficiency of WO_{3-x} resulting in insignificant enhancement caused by the introduction of $K_2Cr_2O_7$.

Based on the above analysis, the bulk oxygen vacancy has optimized the photodegradation mechanism of CBZ by WO_3. The oxygen-vacancy-free sample mainly oxidizes the CBZ by the photoexcited hole (h^+) (Figure 9a), requiring the CBZ to be adsorbed and cause low activity. By contrast, the bulk oxygen vacancy dominating WO_3 mainly produces $\cdot OH$ or $\cdot O^{2-}$ to degrade CBZ; the stronger oxidization power of radicals and their ability to migrate to the solution is beneficial to the degradation of CBZ (Figure 9b).
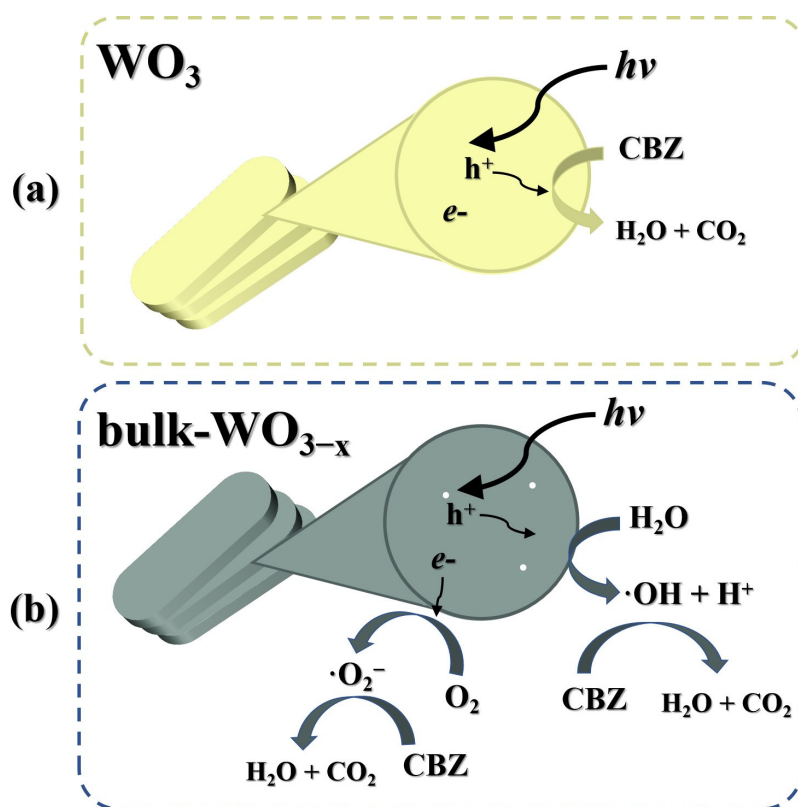
Figure 9. Illustration of photocatalytic mechanism of (**a**) WO_3 and (**b**) bulk-WO_{3-x}.

4. Conclusions

In summary, introduction of oxygen vacancy can improve photoelectric properties and photocatalytic degradation performance of WO_3 samples. The photocurrent density and degradation efficiency of WO_{3-x} increase firstly, followed by diminishing, along with an increase in the proportion of oxygen vacancy. The bulk and surface oxygen vacancies are produced in WO_{3-x} just after thermal treatment. It is found that surface oxygen vacancies would be recovered when WO_{3-x} was oxygen-exposed, resulting in bulk oxygen vacancies dominating WO_{3-x}, whose photocatalytic degradation performance even shows further improvement. Therefore, both proportion and location distribution of oxygen vacancy could exert different influences on the photocatalytic performance of WO_{3-x}. The recovered

behavior of surface oxygen vacancy and more essential influence of bulk oxygen vacancy deserve to be further studied. The CBZ degradation mechanism was compared between WO_3 and bulk oxygen vacancies dominating WO_{3-x}. The results suggest that improvement in photocatalytic degradation may be due to the generation of OH radicals and superoxide radicals. The results of this study could potentially broaden our understanding of the role of oxygen vacancies and provide optimal directions and methods for oxygen vacancy regulation for photocatalysts.

Supplementary Materials: The following supporting information can be downloaded at: https://www.mdpi.com/article/10.3390/nano14110923/s1, Figure S1: The pseudo first-order kinetic fitting curves of as-prepared samples; Figure S2: The pseudo first-order kinetic fitting curves of WO_{3-x} and bulk-WO_{3-x}.

References

1. Zhao, T.; Xing, Z.; Xiu, Z.; Li, Z.; Chen, P.; Zhu, Q.; Zhou, W. Synergistic effect of surface plasmon resonance, Ti^{3+} and oxygen vacancy defects on $Ag/MoS_2/TiO_{2-x}$ ternary heterojunctions with enhancing photothermal catalysis for low-temperature wastewater degradation. *J. Hazard. Mater.* **2019**, *364*, 117–124. [CrossRef] [PubMed]
2. Zhao, H.; Liu, X.; Dong, Y.; Xia, Y.; Wang, H. A special synthesis of BiOCl photocatalyst for efficient pollutants removal: New insight into the band structure regulation and molecular oxygen activation. *Appl. Catal. B Environ.* **2019**, *256*, 117872. [CrossRef]
3. Wang, H.; Zhang, L.; Chen, Z.; Hu, J.; Li, S.; Wang, Z.; Liu, J.; Wang, X. Semiconductor heterojunction photocatalysts: Design, construction, and photocatalytic performances. *Chem. Soc. Rev.* **2014**, *43*, 5234–5244. [CrossRef] [PubMed]
4. Zhang, W.; Li, G.; Liu, H.; Chen, J.; Ma, S.; An, T. Micro/nano-bubble assisted synthesis of Au/TiO_2@CNTs composite photocatalyst for photocatalytic degradation of gaseous styrene and its enhanced catalytic mechanism. *Environ. Sci. Nano* **2019**, *6*, 948–958. [CrossRef]
5. Feng, Y.; Li, H.; Ling, L.; Yan, S.; Pan, D.; Ge, H.; Li, H.; Bian, Z. Enhanced Photocatalytic Degradation Performance by Fluid-Induced Piezoelectric Field. *Environ. Sci. Technol.* **2018**, *52*, 7842–7848. [CrossRef] [PubMed]
6. Han, N.; Wang, S.; Yao, Z.; Zhang, W.; Zhang, X.; Zeng, L.; Chen, R. Superior three-dimensional perovskite catalyst for catalytic oxidation. *EcoMat* **2020**, *2*, e12044. [CrossRef]
7. Jiang, M.; Zhang, M.; Wang, L.; Fei, Y.; Wang, S.; Núñez-Delgado, A.; Bokhari, A.; Race, M.; Khataee, A.; Klemeš, J.J.; et al. Photocatalytic degradation of xanthate in flotation plant tailings by TiO_2/graphene nanocomposites. *Chem. Eng. J.* **2022**, *432*, 134104. [CrossRef]
8. Kim, J.; Lee, C.; Choi, W. Platinized WO_3 as an Environmental Photocatalyst that Generates OH Radicals under Visible Light. *Environ. Sci. Technol.* **2010**, *44*, 6849–6854. [CrossRef] [PubMed]
9. Wang, Y.; Cai, J.; Wu, M.; Chen, J.; Zhao, W.; Tian, Y.; Ding, T.; Zhang, J.; Jiang, Z.; Li, X. Rational construction of oxygen vacancies onto tungsten trioxide to improve visible light photocatalytic water oxidation reaction. *Appl. Catal. B Environ.* **2018**, *239*, 398–407. [CrossRef]
10. Li, Y.; Tang, Z.; Zhang, J.; Zhang, Z. Defect Engineering of Air-Treated WO_3 and Its Enhanced Visible-Light-Driven Photocatalytic and Electrochemical Performance. *J. Phys. Chem. C* **2016**, *120*, 9750–9763. [CrossRef]
11. Mi, Q.; Zhanaidarova, A.; Brunschwig, B.; Gray, H.B.; Lewis, N.S. A quantitative assessment of the competition between water and anion oxidation at WO_3 photoanodes in acidic aqueous electrolytes. *Energy Environ. Sci.* **2012**, *5*, 5694–5700. [CrossRef]
12. Wu, J.; Qiao, P.; Li, H.; Ren, L.; Xu, Y.; Tian, G.; Li, M.; Pan, K.; Zhou, W. Surface-oxygen vacancy defect-promoted electron-hole separation of defective tungsten trioxide ultrathin nanosheets and their enhanced solar-driven photocatalytic performance. *J. Colloid Interface Sci.* **2019**, *557*, 18–27. [CrossRef] [PubMed]

13. Koo, B.; Ahn, H. Fast-switching electrochromic properties of mesoporous WO_3 films with oxygen vacancy defects. *Nanoscale* **2017**, *9*, 17788–17793. [CrossRef] [PubMed]

14. Petruleviciene, M.; Juodkazyte, J.; Parvin, M.; Tereshchenko, A.; Ramanavicius, S.; Karpicz, R.; Samukaite-Bubniene, U.; Ramanavicius, A. Tuning the Photo-Luminescence Properties of WO_3 Layers by the Adjustment of Layer Formation Conditions. *Materials* **2020**, *13*, 2814. [CrossRef]

15. Shi, W.; Li, H.; Chen, J.; Lv, X.; Shen, Y. Hierarchical WO_3 nanoflakes architecture with enhanced photoelectrochemical activity. *Electrochim. Acta* **2017**, *225*, 473–481. [CrossRef]

16. Solarska, R.; Królikowska, A.; Augustyński, J. Silver Nanoparticle Induced Photocurrent Enhancement at WO_3 Photoanodes. *Angew. Chem. Int. Ed.* **2010**, *49*, 7980–7983. [CrossRef]

17. Liu, G.; Han, J.; Zhou, X.; Huang, L.; Zhang, F.; Wang, X.; Ding, C.; Zheng, X.; Han, H.; Li, C. Enhancement of visible-light-driven O_2 evolution from water oxidation on WO_3 treated with hydrogen. *J. Catal.* **2013**, *307*, 148–152. [CrossRef]

18. Moulzolf, S.; Ding, S.; Lad, R. Stoichiometry and microstructure effects on tungsten oxide chemiresistive films. *Sens. Actuators B Chem.* **2001**, *77*, 375–382. [CrossRef]

19. Solarska, R.; Królikowska, A.; Augustyński, J. Silver Nanoparticle Induced Photocurrent Enhancement at WO_3 Photoanodes. *Angew. Chem. Int. Ed.* **2010**, *122*, 8152–8155. [CrossRef]

20. Liu, Q.; Wang, F.; Lin, H.; Xie, Y.; Tong, N.; Lin, J.; Zhang, X.; Zhang, Z.; Wang, X. Surface oxygen vacancy and defect engineering of WO3 for improved visible light photocatalytic performance. *Catal. Sci. Technol.* **2018**, *8*, 4399–4406. [CrossRef]

21. Long, R.; English, N. Various $3d$-$4f$ spin interactions and field-induced metamagnetism in the Cr^{5+} system $DyCrO_4$. *Phys. Rev. B* **2011**, *83*, 024416. [CrossRef]

22. Ansari, S.; Khan, M.; Kalathil, S.; Nisar, A.; Lee, J.; Cho, M.H. Oxygen vacancy induced band gap narrowing of ZnO nanostructures by an electrochemically active biofilm. *Nanoscale* **2013**, *5*, 9238–9246. [CrossRef] [PubMed]

23. Linsebigler, A.; Lu, G. Photocatalysis on TiO_2 Surfaces: Principles, Mechanisms, and Selected Results. *Chem. Rev.* **1995**, *95*, 735–758. [CrossRef]

24. Cai, J.; Zhu, Y.; Liu, D.; Meng, M.; Hu, Z.; Jiang, Z. Synergistic Effect of Titanate-Anatase Heterostructure and Hydrogenation-Induced Surface Disorder on Photocatalytic Water Splitting. *ACS Catal.* **2015**, *5*, 1708–1716. [CrossRef]

25. Schmid, M.; Shishkin, M.; Kresse, G.; Napetschnig, E.; Varga, P.; Kulawik, M.; Nilius, N.; Rust, H.-P.; Freund, H.-J. Oxygen-Deficient Line Defects in an Ultrathin Aluminum Oxide Film. *Phys. Rev. Lett.* **2006**, *97*, 046101. [CrossRef] [PubMed]

26. Weinhardt, L.; Blum, M.; Bär, M.; Heske, C.; Cole, B.; Marsen, B.; Miller, E.L. Electronic Surface Level Positions of WO_3 Thin Films for Photoelectrochemical Hydrogen Production. *J. Phys. Chem. C* **2008**, *112*, 3078–3082. [CrossRef]

27. Ramanavicius, S.; Petruleviciene, M.; Juodkazyte, J.; Grigucevičienė, A.; Ramanavičius, A. Selectivity of Tungsten Oxide Synthesized by Sol-Gel Method Towards Some Volatile Organic Compounds and Gaseous Materials in a Broad Range of Temperatures. *Materials* **2020**, *13*, 523. [CrossRef] [PubMed]

28. Zheng, X.; Dong, X.; Zhang, S.; Yang, J. Defect-induced ferromagnetism in $W_{18}O_{49}$ nanowires. *J. Alloys Compd.* **2020**, *818*, 152894. [CrossRef]

29. Liu, Y.; Yao, W.; Lin, J. Improved photoelectrocatalytic performances over electrochemically reduced WO3: Implications of oxygen vacancies. *Phys. Chem. Chem. Phys.* **2023**, *25*, 15248–15256. [CrossRef]

30. Hu, Z.; Xu, M.; Shen, Z.; Yu, J. A nanostructured chromium(III) oxide/tungsten(VI) oxide p–n junction photoanode toward enhanced efficiency for water oxidation. *J. Mater. Chem. A* **2015**, *3*, 14046–14053. [CrossRef]

31. Zhang, T.; Zhao, K.; Yu, J.; Jin, J.; Qi, Y.; Li, H.; Hou, X.; Liu, G. Photocatalytic water splitting for hydrogen generation on cubic, orthorhombic, and tetragonal $KNbO_3$ microcubes. *Nanoscale* **2013**, *5*, 8375–8383. [CrossRef]

32. Pan, X.; Yang, M.; Fu, X.; Zhang, N.; Xu, Y.-J. Defective TiO_2 with oxygen vacancies: Synthesis, properties and photocatalytic applications. *Nanoscale* **2013**, *5*, 3601–3614. [CrossRef] [PubMed]

33. Li, W.; Da, P.; Zhang, Y.; Wang, Y.; Lin, X.; Gong, X.; Zheng, G. WO_3 Nanoflakes for Enhanced Photoelectrochemical Conversion. *ACS Nano* **2014**, *8*, 11770–11777. [CrossRef] [PubMed]

34. Zhao, C.; Kong, X.; Liu, X.; Tu, L.; Wu, F.; Zhang, Y.; Liu, K.; Zeng, Q.; Zhang, H. Li^+ ion doping: An approach for improving the crystallinity and upconversion emissions of $NaYF_4$:Yb^{3+}, Tm^{3+} nanoparticles. *Nanoscale* **2013**, *5*, 8084–8089. [CrossRef] [PubMed]

35. Zhang, R.; Ning, F.; Xu, S.; Zhou, L.; Shao, M.; Wei, M. Oxygen vacancy engineering of WO_3 toward largely enhanced photoelectrochemical water splitting. *Electrochim. Acta* **2018**, *274*, 217–223. [CrossRef]

36. Yang, X.; Wolcott, A.; Wang, G.; Sobo, A.; Fitzmorris, R.C.; Qian, F.; Zhang, J.Z.; Li, Y. Nitrogen-Doped ZnO Nanowire Arrays for Photoelectrochemical Water Splitting. *Nano Lett.* **2009**, *9*, 2331–2336. [CrossRef] [PubMed]

37. Wolcott, A.; Smith, W.; Kuykendall, T.; Zhao, Y.; Zhang, J.Z. Photoelectrochemical Water Splitting Using Dense and Aligned TiO_2 Nanorod Arrays. *Small* **2009**, *5*, 104–111. [CrossRef]

38. Yang, Y.; Zhang, C.; Huang, D.; Zeng, G.; Huang, J.; Lai, C.; Zhou, C.; Wang, W.; Guo, H.; Xue, W.; et al. Boron nitride quantum dots decorated ultrathin porous g-C_3N_4: Intensified exciton dissociation and charge transfer for promoting visible-light-driven molecular oxygen activation. *Appl. Catal. B Environ.* **2019**, *245*, 87–99. [CrossRef]

39. Rahimnejad, S.; He, J.; Pan, F.; Lee, X.; Chen, W.; Wu, K.; Xu, G.Q. Enhancement of the photocatalytic efficiency of WO_3 nanoparticles via hydrogen plasma treatment. *Mater. Res. Express* **2014**, *1*, 045044. [CrossRef]

40. Ma, J.; Wang, C.; He, H. Enhanced photocatalytic oxidation of NO over g-C_3N_4-TiO_2 under UV and visible light. *Appl. Catal. B Environ.* **2016**, *184*, 28–34. [CrossRef]